

Evolution of γ' Precipitation During the Early Stages of Industrial Forging of a Nickel-Based Superalloy



A. COYNE-GRELL, J. BLAIZOT, S. RAHIMI, I. VIOLATOS, S. NOUVEAU, C. DUMONT, A. NICOLAY, and N. BOZZOLO

A sample of the Ni-based superalloy AD730 was heat treated at a supersolvus temperature (1160 °C) then slowly cooled through the solvus temperature (1110 °C) at 10 °C/hr down to 1080 °C, *i.e.*, a rate representative of the cooling conditions of an industrial-scale billet undergoing controlled cooling. The γ' precipitate distribution which forms during this cooling was investigated, and a mix of continuous and discontinuous precipitation was found. The discontinuous γ' precipitates were imaged using 3D tomography, and were shown to present very different sizes, morphologies, and aspect ratios when observed in different 2D imaging planes. The interaction between different populations of γ' precipitate and recrystallization was investigated, and it was found that the discontinuous precipitates present more of a barrier to recrystallization than the continuous ones. This has been explained based on the different inter-precipitate spacings observed for the two populations. In addition to these γ' precipitates which form during slow cooling, a fine and dense distribution of approximately spherical γ' precipitates was found to form dynamically, during subsequent subsolvus forging, within unrecrystallized grains.

<https://doi.org/10.1007/s11661-022-06878-w>
© The Author(s) 2022

I. INTRODUCTION

CONTROL of the γ' precipitation is central to the metallurgy of nickel-based superalloys. These precipitates are responsible, to a significant extent, for the excellent high temperature strength of such alloys through the order strengthening mechanism.^[1] The effect of volume fraction, size, and distribution of this phase on alloys' yield strength, fatigue life, and creep resistance has been well investigated.^[2–5] As such, heat treatments to control the γ' distribution are typically applied after the end of closed die forging operations. The influence of different heat treatments on the formation, coarsening, and dissolution of hardening γ' -precipitates have also been extensively studied.^[6–10]

However, as well as their influence on in-service properties, γ' precipitates can also strongly affect microstructural evolution during the production of

superalloy billets and further forging operations; for instance, the progress of recrystallization during subsolvus forging. The size and inter-particle spacing of a precipitate distribution can affect the mechanisms and kinetics of recrystallization (*i.e.*, the extent of recrystallization as a function of strain).^[11,12]

In Udimet 720, it has been shown that during two-stroke forging, applying an intermediate heat treatment, which promotes coarsening of secondary γ' , between the two forging strokes can enhance the recrystallization level achieved.^[12] A similar observation has been made in AD730; in a sample with heterogeneous γ' precipitation, regions with a coarser and sparser distribution of γ' precipitates showed faster recrystallization kinetics (*i.e.*, higher recrystallization levels as a function of strain) than regions with a finer and denser distribution.^[11]

In a billet conversion process, the γ' precipitates which are present at the start of subsolvus forging are those that have formed during *slow* cooling through the solvus. In the case of industrial-scale billets undergoing controlled cooling, these *slow* cooling rates are on the order of 10 °C/h. Such *slow* cooling rates are rarely considered in lab scale trials, where *slow* cooling rates are typically, at lowest, on the order of 0.1 °C/s,^[10,13] *i.e.*, at least a factor of 36 faster than the *slow* cooling rates experienced by industrial-scale components.

These *slow* cooling rates can be expected to have two effects on γ' precipitation. Firstly, given the ample time

A. COYNE-GRELL, S. RAHIMI, and I. VIOLATOS are with the Advanced Forming Research Centre (AFRC), University of Strathclyde, 85 Inchinnan Drive, Inchinnan PA4 9LJ, UK. Contact e-mail: angus.coyne@strath.ac.uk J. BLAIZOT, S. NOUVEAU, and C. DUMONT are with the Aubert & Duval, Site des Ancizes, BP1, 63770 Les Ancizes Cedex, France. A. NICOLAY and N. BOZZOLO are with the MINES Paris, PSL – Research University, CEMEF – Centre de Mise en Forme des Matériaux, Sophia – Antipolis, France. Manuscript submitted July 31, 2022; accepted October 20, 2022.

for coarsening and low levels of supersaturation, precipitates are expected to coarsen and develop an octodendritic shape, *i.e.*, a shape having eight arms extended along the $\langle 111 \rangle$ directions. This shape has been observed to form during slow cooling, and is the result of a coarsening process in which γ' precipitate shape evolves from a sphere, to a cube, to an octocube, and eventually to an octodendrite.^[14,15]

Secondly, slow cooling rates in the vicinity of the solvus temperature allow grain boundaries to move over larger distances, as their mobility is higher at higher temperatures; high grain boundary mobility has been identified as the main factor favoring the formation of discontinuous “fan-type” γ' precipitates by Atrazhev *et al.*^[16] As Atrazhev *et al.* point out, in polycrystalline samples, there will be a wide range of grain boundary mobility, so even during slow cooling a mixture of continuous (*i.e.*, octodendritic) and discontinuous γ' precipitation may be expected. The interactions of these two types of γ' precipitate with recrystallization during subsequent hot forging within a single sample have not yet been investigated, although such heterogeneous microstructures are representative of the early intermediate stages of ingot to billet conversion.

The main aims of this work are thus twofold. Firstly, to characterize the γ' precipitate distribution which forms during *slow* cooling (*i.e.*, at industrially relevant rates, on the order of 10 °C/h) of a nickel-based superalloy. Such a γ' precipitate distribution is representative of the microstructure at the early stages of open die forging. Secondly, to examine the interaction of

this γ' precipitate distribution with recrystallization during a subsolvus forging operation.

II. MATERIAL AND METHODS

A. Material and Thermomechanical Treatment

AD730 billet material^[17] was supplied by Aubert & Duval as the starting material for this work. This material had been triple melted (*i.e.*, vacuum induction melted, electro-slag re-melted, and vacuum arc re-melted) and had undergone super and subsolvus forging and upsetting steps. The nominal chemical composition of this alloy is provided in Table I. Cylinder-shaped samples with diameters of 50 mm and lengths of 75 mm were prepared from billet material along the longitudinal direction.

The thermomechanical treatment schematically shown in Figure 1 was applied to these cylinders. Water quenching was performed at various points along the treatment to progressively observe microstructure evolution. In this way, 4 samples (A–D) were produced. The first three (A–C) allow γ' precipitation during *slow* cooling to be investigated, and the fourth (D) shows how recrystallization interacts with the γ' precipitates so developed.

Heat treatments were carried out in two furnaces. Samples were first held for 40 min at 1160 °C in a Carbolite RHF 1400 furnace, and were then quickly transferred to a Carbolite GPC furnace at 1125 °C,

Table I. Nominal Chemical Composition of AD730 in Wt Pct

Element	Ni	Fe	Cr	Co	Mo	W	Al	Ti	Nb	C	B	Zr
Wt Pct	bal	4.0	15.7	8.5	3.1	2.7	2.25	3.4	1.1	0.02	0.01	0.03

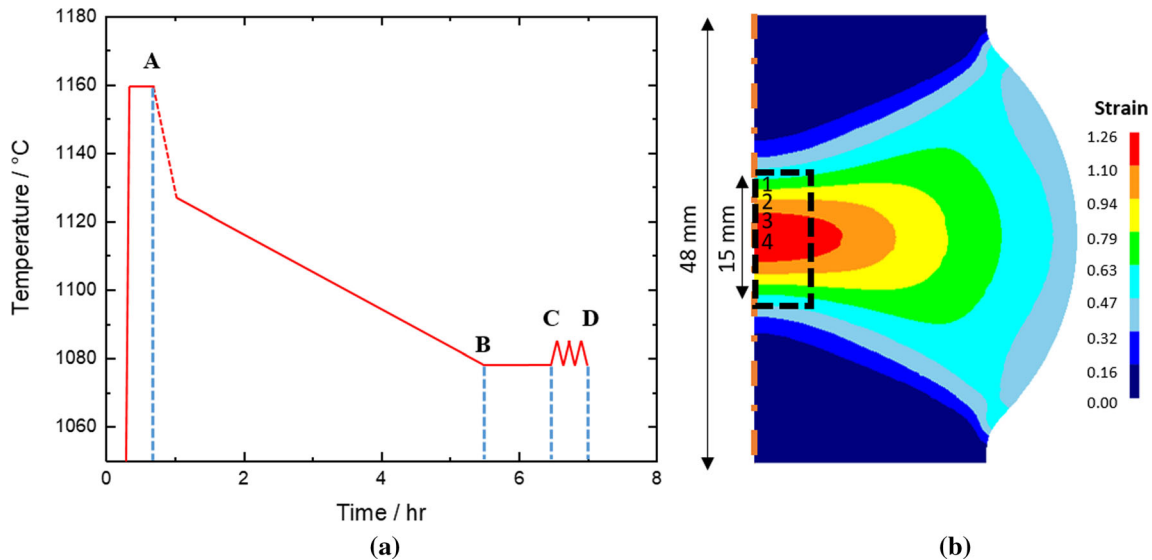


Fig. 1—(a) A schematic plot of the thermomechanical path applied to the cylindrical samples, and (b) the predicted strain distribution by finite element simulation in the deformed sample D. Note that four locations from which large area EBSD maps were subsequently taken are shown.

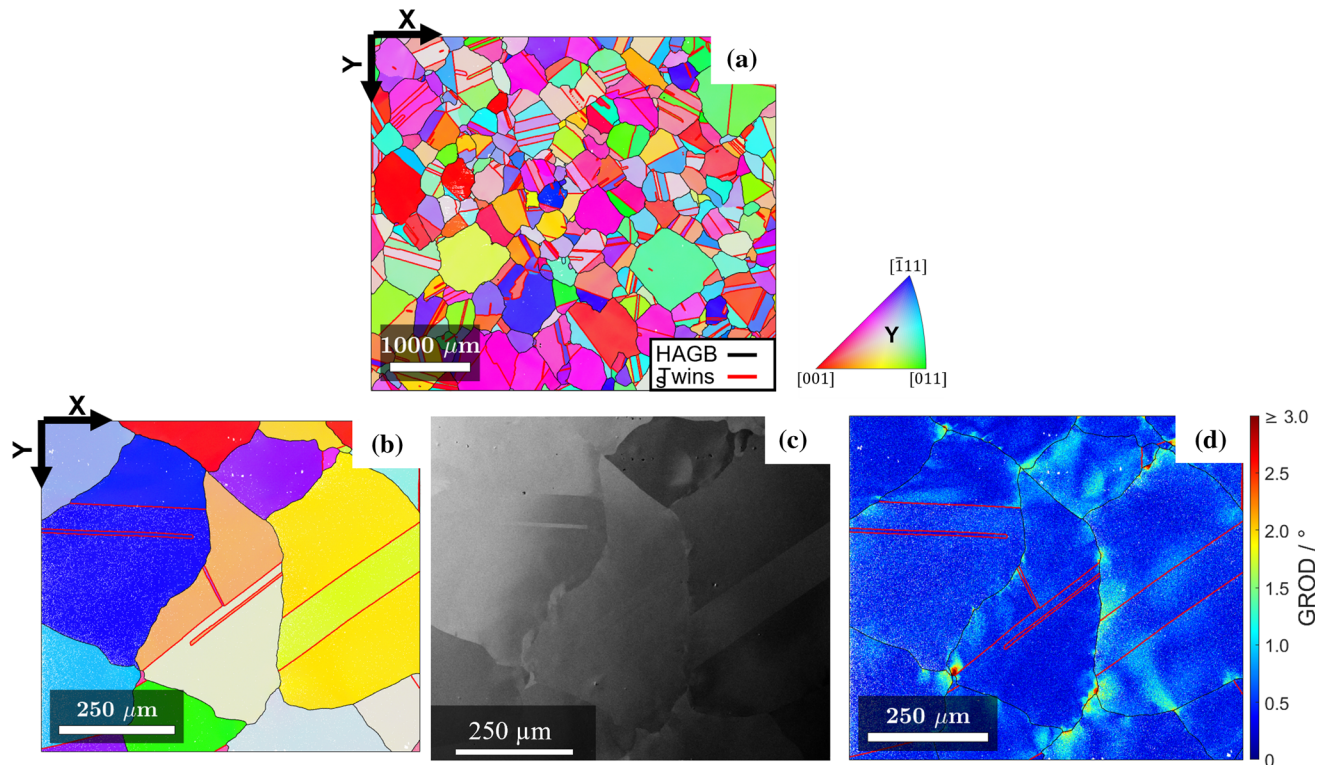


Fig. 2—Overview of the microstructure of sample A. (a) A low-magnification IPF Y map showing large, approximately equiaxed grains, (b to d) higher magnification images of a region in sample A where the γ matrix shows intragranular contrast variations in BSE images (c), which correspond to low misorientation gradients indicated by the low values in the GROD map in (d).

which was programmed to cool at a rate of 10 °C/h down to 1080 °C, at which temperature the samples were held for 1 h. Sample A was quenched right at the end of the first holding at 1160 °C. Sample B was quenched as soon as it reached 1080 °C at the end of the controlled cooling, and sample C after one hour at 1080 °C. The fourth sample (D) followed the whole same thermal path as sample C and was then transferred to a 500 T hydraulic press with flat dies, which had been pre-heated to 450 °C and lubricated using graphite. The sample was placed on the lower die and compressed by the upper die, which moved down at a constant speed of 3 mm/s. The sample was compressed for 9 s, corresponding to a height reduction of 27 mm and a macroscopic average true strain of 0.45. After compression, sample D was removed from the dies and quenched in water. The whole compression process was recorded, allowing accurate determination of dwell time on the lower die before compression, and the delay time between the end of compression and quenching.

B. Finite Element (FE) Analysis

To obtain a semi-quantitative estimate of the strain distribution in the deformed sample, the DEFORM software was used to perform a 2D axisymmetric FE simulation of the compression test conducted on the sample (*i.e.*, sample D). A heat transfer coefficient of 11 mW/m²K and a friction coefficient of 0.3 between the dies and the sample were implemented, as per the

software's suggested values for lubricated hot forging. A Taylor–Quinney factor of 0.9 was used, which is a typical approximation for the fraction of mechanical work converted into heat during deformation.^[18] The workpiece shown in Figure 1(b), which represents one half of the sample, was meshed into 3143 elements.

The shape of the sample after deformation was measured and compared with the shape predicted by the FE simulation. The sample's maximum diameter was measured to be 70 mm, compared with 68.7 mm predicted by the FE model. The close match suggests that the chosen values of friction and heat transfer coefficient were reasonably good.

C. Microstructure Analysis

Microstructural examinations were conducted *via* scanning electron microscopy. A 12 × 15 mm plate was cut out from the center of each sample using wire electrical discharge machining. Samples were then mounted in conductive Bakelite and ground and polished to a mirror finish, then subjected to a final vibratory polishing for 16 h using 0.02 μm colloidal silica suspension. Backscattered electron (BSE) images and electron backscatter diffraction (EBSD) orientation maps were acquired using an FEI Quanta 250 field emission gun scanning electron microscope (FEG-SEM) interfaced with a Nordlys Max 2 EBSD detector and the Oxford AZtec software.

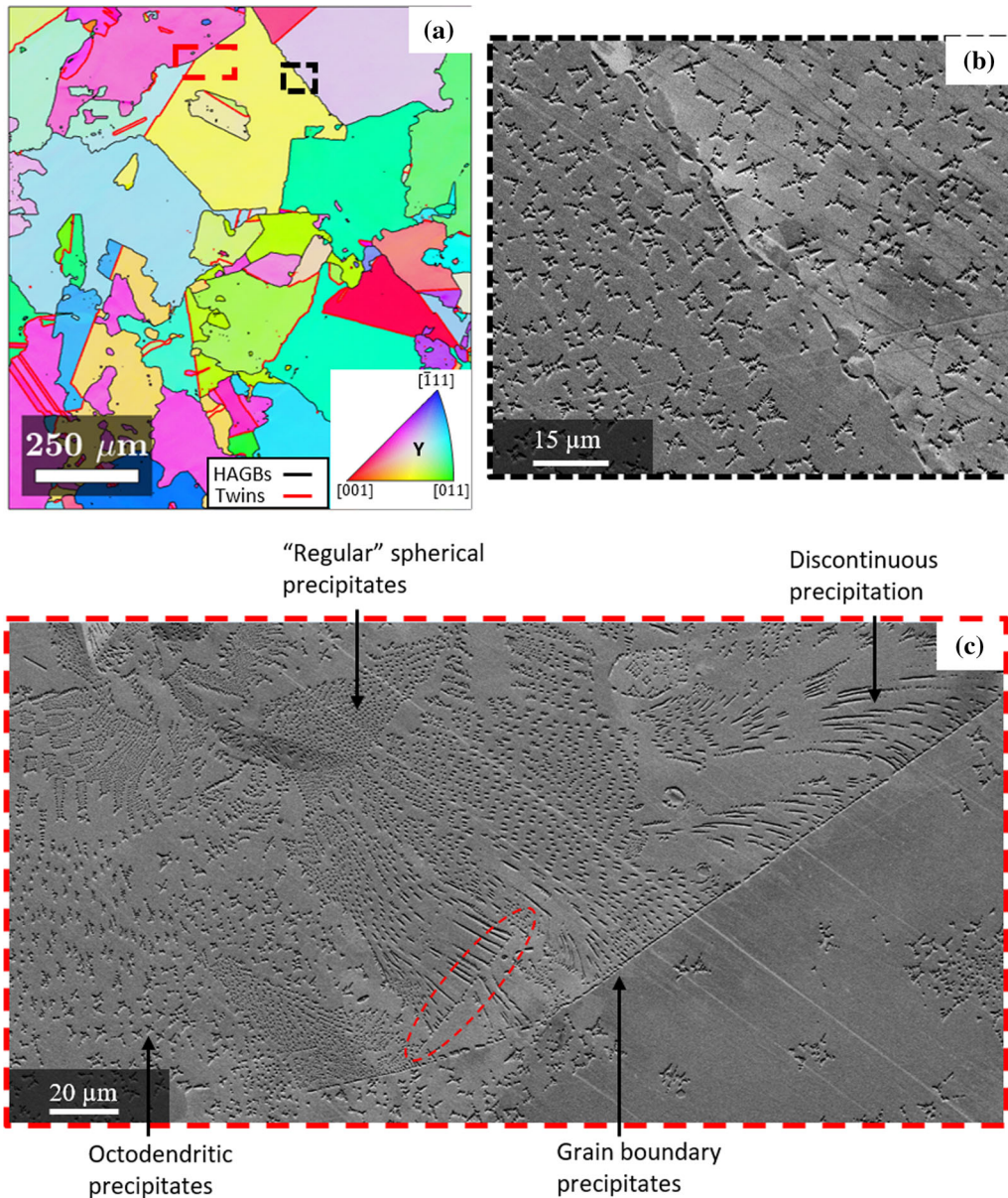


Fig. 3—(a) A 1 mm² IPF Y map of sample C, with (b to c) corresponding FSE images from selected areas which highlight the different γ' precipitate morphologies. γ' Precipitation along a grain boundary is highlighted in (b) and four different morphologies can be identified from the 2D micrograph in (c).

For sample D which underwent deformation after the heat treatment, large area (roughly 1 mm²) EBSD maps were taken at four different locations along the axis of the deformed cylinder, corresponding to different local strain levels [see Figure 1(b) for the location of the EBSD maps]. This large map was created by merging together 20 smaller maps, collected using a 1 μm step size. A similar map was taken from sample C, along with a corresponding merged forward scattered electron (FSE) image.

To examine the 3D shape of γ' precipitates, focused ion beam-scanning electron microscope (FIB-SEM) tomography was used. The microscope used was a Tescan FERA3 FEG-SEM equipped with a Xe + Plasma-FIB column. A region of interest was selected

and 0.1- μm -thick slices were consecutively milled away, and a BSE image was collected in between each slice. FIB slicing was done using an accelerating voltage of 30 kV and a beam current of 100 nA. The resulting stack of 2D images were then segmented to separate out γ' precipitates from the γ matrix using the Pixel classification workflow of ilastik, an image analysis software that leverages machine learning.^[19]

In the pixel classification workflow, the user labels pixels to assign them to one of two classes (in this case identifying whether they belong to the γ or γ' phase). Based on these labels, dividing lines are drawn in the feature space which separate pixels with the different labels. Here, the feature space is a 3D space, with axes which are the pixel properties intensity, edge, and

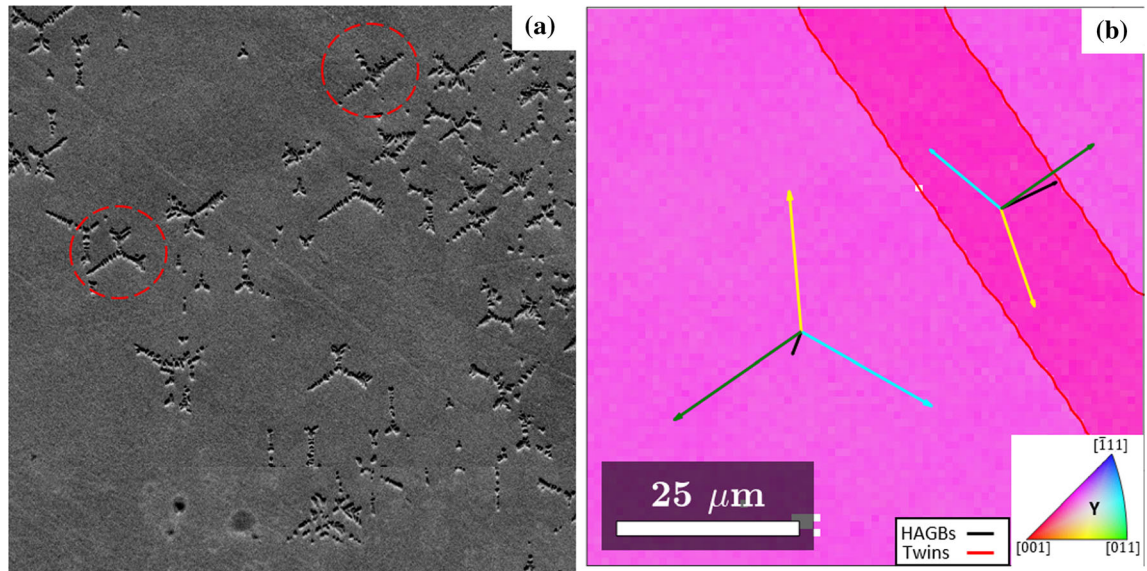


Fig. 4—(a) An FSE image and (b) its corresponding IPF Y map of a region containing octodendritic γ' precipitates in sample C. In (b), four $\langle 111 \rangle$ type directions are overlaid. Note that the region contains two twin boundaries which are not highly visible in the BSE image, but their effect on octodendrite arm direction can be seen, as shown by the two γ' precipitates highlighted.

texture. These labels thus act as training data. For the FIB-SEM image analysis, a few images from the stack of images were partially labeled, and the remaining images were visually inspected to check the quality of the segmentation. Segmentation errors could be corrected by adding labels to incorrectly segmented pixels, and in this way the whole stack could be segmented very accurately with relatively little labeling (a total of about 5 images were partially labeled). Additional information on pixel classification and other workflows in ilastik can be found in reference 20.

This stack of binary 2D images was reconstructed into a 3D image and visualized using ImageJ.^[20] Data were extracted from two volumes, with dimensions of $53.0 \mu\text{m} \times 68.2 \mu\text{m} \times 52.5 \mu\text{m}$ and $41.0 \mu\text{m} \times 63.9 \mu\text{m} \times 52.9 \mu\text{m}$, from samples B and D, respectively. From these two volumes, two sub-volumes which displayed minimal curtaining effect were extracted and analyzed.

III. RESULTS

A. γ' Precipitation on Slow Cooling

Figure 2(a) shows a low-magnification IPF Y color-coded map for sample A (the Y direction is parallel to the sample's cylindrical axis). Discounting twin boundaries, the average equivalent circle diameter of the grains in this micrograph is $268 \pm 215 \mu\text{m}$. Only γ' precipitates which formed during the water quenching are present, and these were too fine to be resolved at these low magnifications.

Figures 2(b) through (d) show sample A at a higher magnification, where there is evidence of pockets of remnant stored energy, predominantly near to grain boundaries and triple junctions. Regions can indeed be

found where the γ matrix within a single grain shows contrast in BSE images, *e.g.*, Figure 2(c). This is thought to be channeling contrast, likely due to small orientation gradients, which can be an indication of remnant stored energy. These gradients are sufficiently small that they are not apparent in the IPF color-coded map (Figure 2(b)). A grain reference orientation deviation (GROD) plot, which shows the misorientation angle between each pixel in a grain and the average orientation of that grain, is shown in Figure 2(d). This shows that these orientation gradients are indeed rather small, with few points exceeding a GROD of 1° , and these are concentrated around grain boundaries. However, since BSE contrast can be very sensitive to crystal orientation, these gradients are detected in the BSE image.^[21] Such orientation gradients could be due to dislocations which form during water quenching; the formation of such dislocations has been shown in Inconel 718.^[22]

Figure 3 shows the γ' precipitation which has developed in sample C during *slow* cooling from above the solvus temperature and after a 1-h hold at 1080°C . A similar state is observed in sample B, so a separate figure showing the same information has not been included. Figure 3(a) shows an IPF Y map and (b–c) show corresponding FSE images from the highlighted regions. The high-magnification micrograph in (b) shows the grain boundary γ' precipitation at a serrated boundary. The high-magnification micrograph in (c) shows that there appears to be four distinct categories of γ' precipitate, namely: (i) octodendrites, (ii) discontinuous precipitation, (iii) grain boundary precipitates, and (iv) “regular” precipitates which could have formed continuously inside grains.

The grain boundary γ' precipitates shown in Figure 3(c) are at the discontinuous precipitation reaction front, and this boundary is very flat (in this 2D section). The red ellipse in Figure 3(c) shows a

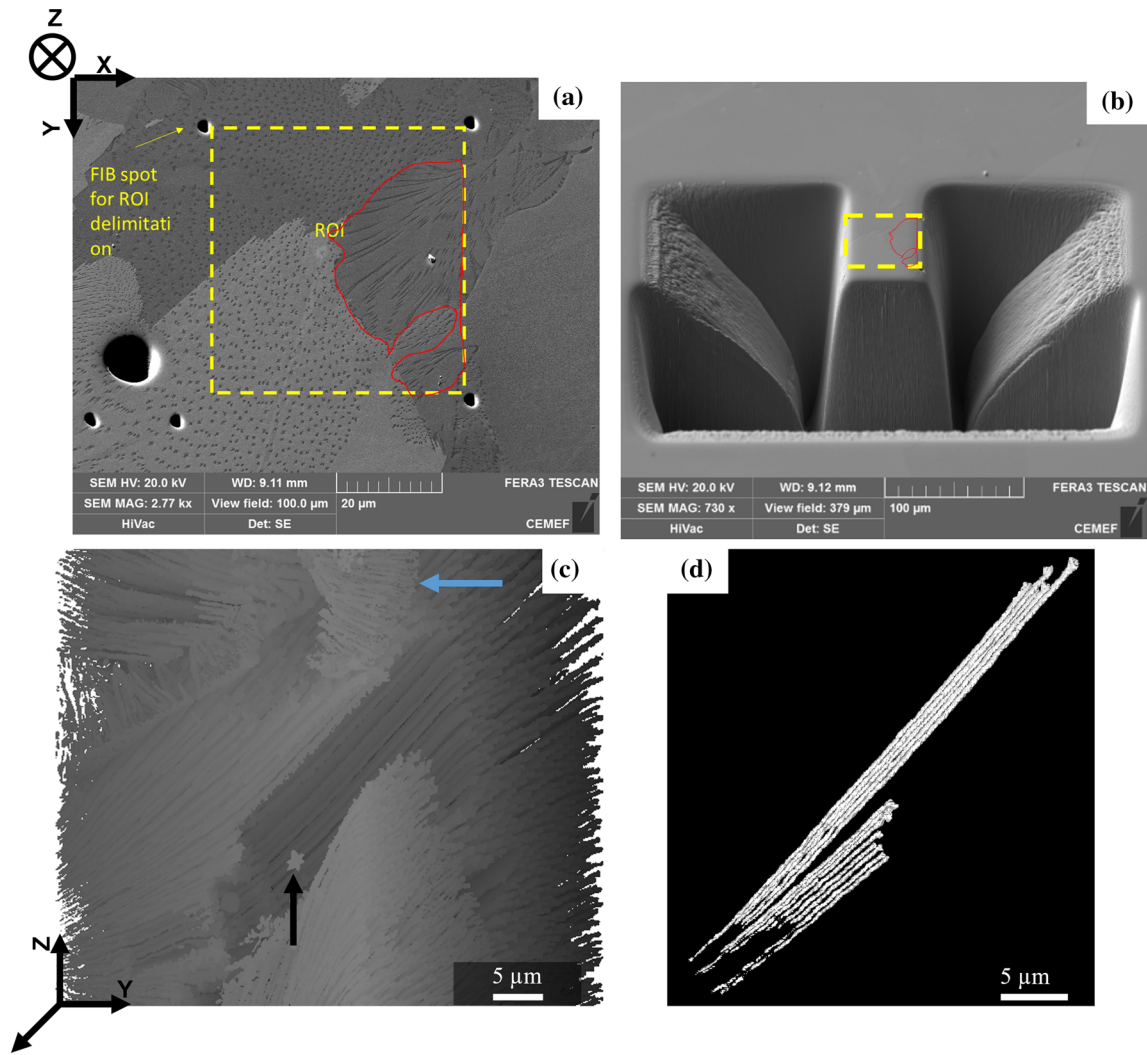


Fig. 5—FIB-SEM tomography to reveal the 3D shape of discontinuous γ' precipitates. (a) A region of interest from sample B, which appears to contain a mixture of approximately cuboidal and discontinuous γ' precipitates. (b) The same region after FIB milling to prepare for serial sectioning. (c) The 3D dataset produced by serial sectioning and image segmentation showing that the region of interest contains almost exclusively discontinuous γ' precipitation with a “spaghetti” morphology (one of the few octodendrites present is highlighted by the black arrow and an example of a fan-type structure is shown by the blue arrow). (d) A selection of discontinuous γ' precipitates, some of which extend throughout the whole investigated volume (Color figure online).

discontinuous precipitation reaction front which is not along a grain boundary, producing a strikingly straight line of intragranular γ' precipitation. Figure 3(b) shows a boundary between two grains containing octodendritic γ' precipitation which is more serrated.

Figure 4 shows that the dendritic arms of the octodendritic γ' precipitates extend along $\langle 111 \rangle$ crystallographic directions of the matrix, as has previously been observed.^[14,15] In Figure 4(b), the $\langle 111 \rangle$ crystallographic directions are indicated as arrows which are the projections of the $\langle 111 \rangle$ directions on to the plane being imaged, hence shorter arrows represent the directions closer to the normal to the surface.

To better investigate the γ' precipitate morphologies highlighted in Figure 3, the region indicated in Figure 5(a) was analyzed in 3D *via* FIB-SEM tomography. This region was identified in sample B, and appears to show two distinct γ' precipitate morphologies in 2D.

There are some discontinuous γ' precipitates (outlined in red), and other γ' precipitates which show a more “regular” approximately cuboidal morphology. A 3D view of the γ' precipitates in Figure 5(a) was obtained by serial sectioning and imaging of a cross section perpendicular to the plane of view in Figure 5(a). An intermediate micrograph taken from the preparation stage of this cross section, before serial sectioning, is shown in Figure 5(b). The acquired 3D view is shown in Figure 5(c), and reveals that, despite the apparently distinct 2D morphologies, almost all the γ' precipitates in the investigated region are discontinuous, with the exception of a few isolated and identifiable octodendrites (one is highlighted with the black arrow). Figures 5(c) and (d) also highlight that the majority of the γ' precipitates have a “spaghetti” shape in 3D, extending through the whole length of the investigated region (*i.e.*, 35 μm). Towards the top of Figure 5(c)

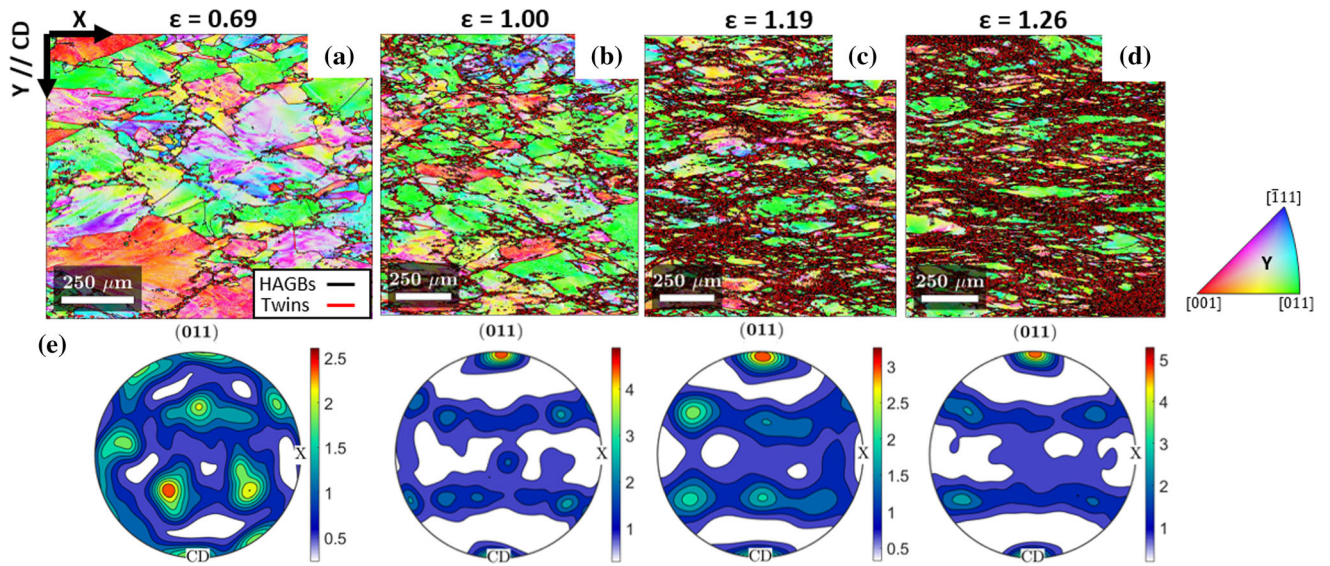


Fig. 6—(a) to (d) Large area IPF maps showing microstructure evolution as a function of strain in sample D, taken from regions 1–4, respectively, highlighted in Fig. 1. (e) $\langle 110 \rangle$ pole density figures for the unrecrystallized grains, corresponding to each strain zone, which show the development of a $\langle 110 \rangle$ fiber texture in the unrecrystallized grains during forging.

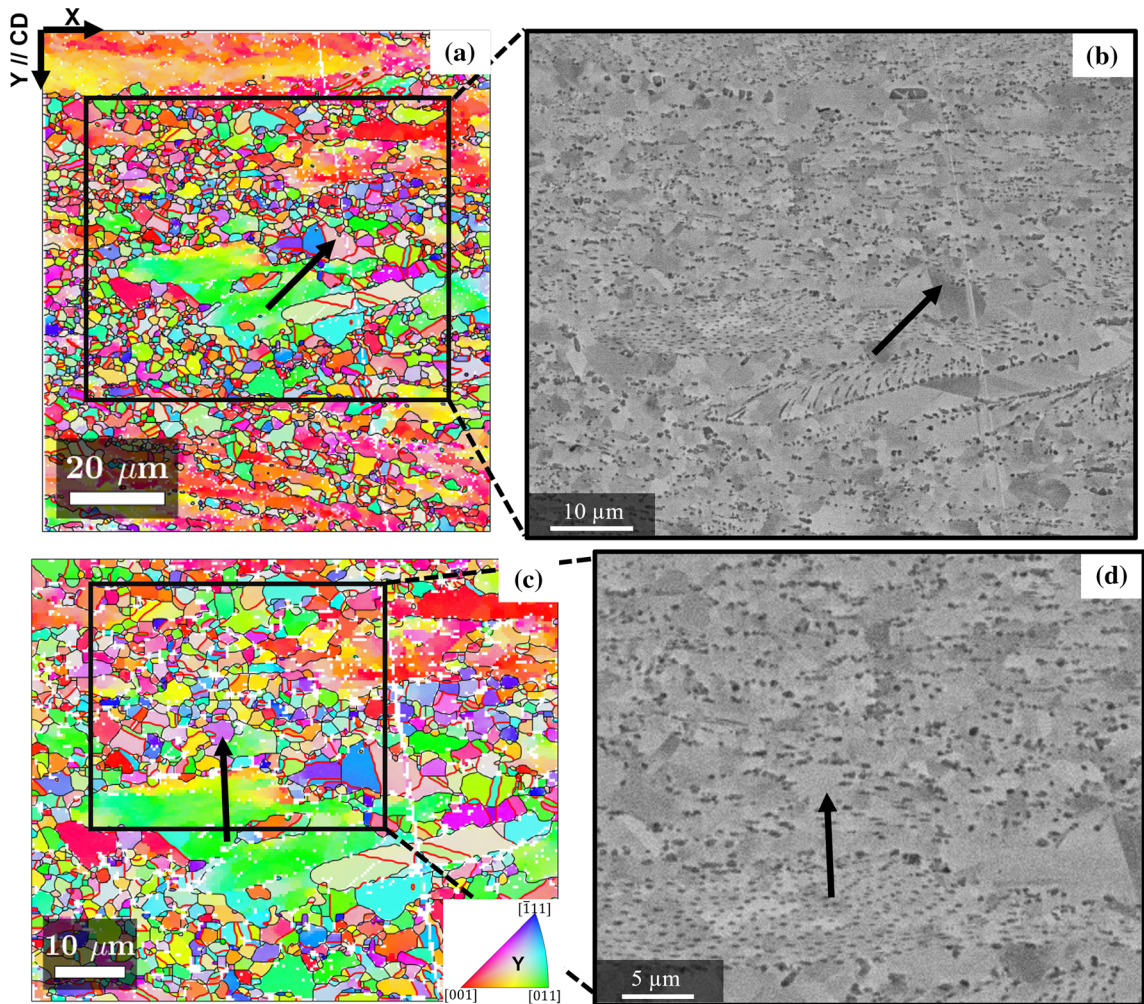


Fig. 7—Recrystallized grains in a region, where $\epsilon \approx 1.26$. An IPF Y map (a) with corresponding BSE image (b), where a relatively large recrystallized grain is highlighted with an arrow; higher magnification views of the same region are shown in (c) and (d), where a smaller recrystallized grain is highlighted.

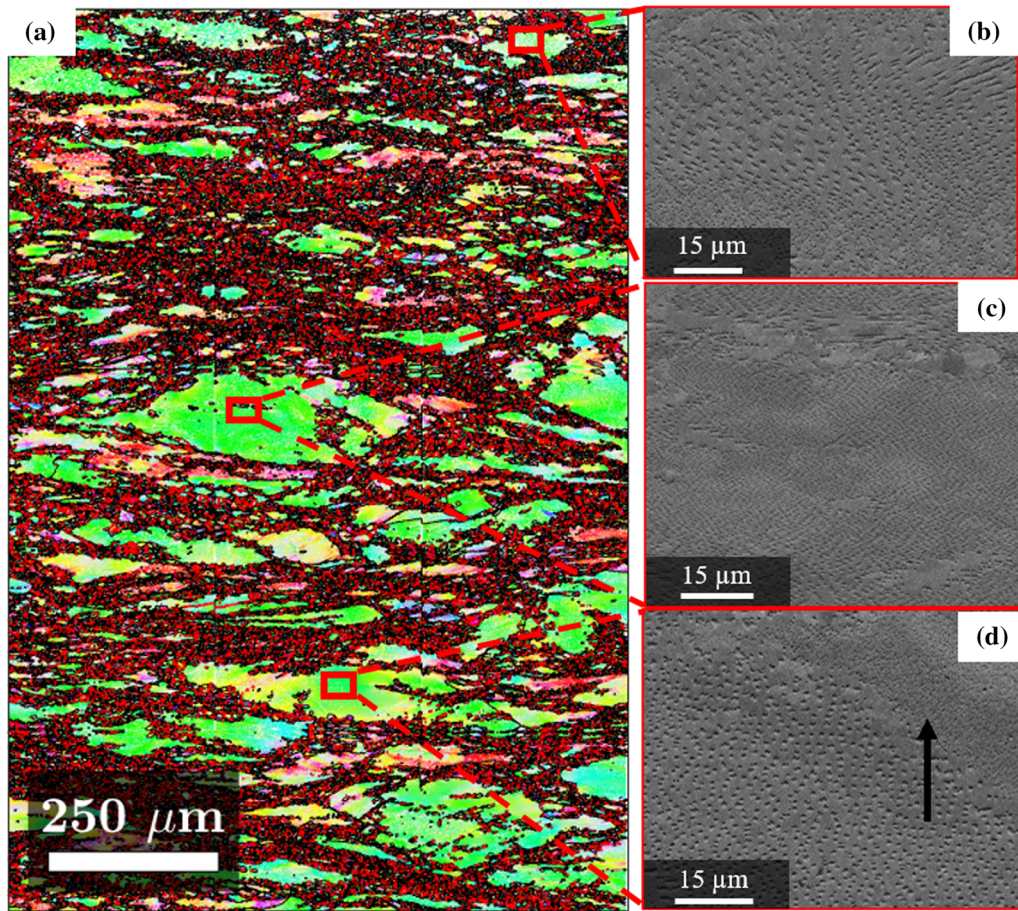


Fig. 8—(a) IPF Y map of a large area from a region of sample D, where $\varepsilon \approx 1.26$, (b) to (d) magnified FSE images of the γ' precipitation in three selected unrecrystallized grains highlighted in (a). Note that an example of a region with very fine spherical γ' precipitates observed only after forging (*i.e.*, formed dynamically) is highlighted by the arrow in (d).

there is a single example of fan-type γ' precipitates (*i.e.*, alternating branches of γ and γ' which appear to originate from a single precipitate behind a curved boundary), shown by the blue arrow. An animated view of the volume in Figure 5(c) is shown in video S1.

B. Microstructure Evolution During Subsolvus Forging

An overview of the progression of recrystallization as a function of strain magnitude in sample D is given by the four IPF color-coded maps in Figure 6. These have been colorized along the compression direction (CD). These show that a typical necklace structure of recrystallized grains has developed around the unrecrystallized ones. The tendency for the unrecrystallized grains to appear green in these maps reflects the $\langle 110 \rangle$ fiber texture which has developed in the unrecrystallized grains during forging. This is further highlighted in the $\{110\}$ pole figures included in Figure 6(e). These show the texture strength for the unrecrystallized grains in multiples of the uniform distribution; here unrecrystallized grains were classified as those grains having

equivalent diameters above $10 \mu\text{m}$. Such a texture is expected in FCC materials during compression.^[23]

The recrystallized grains are highlighted in Figure 7. The larger recrystallized grains, such as the one highlighted in Figures 7(a) and (b), have little to no intragranular γ' precipitation. The same is true for the smaller recrystallized grains, shown in Figures 7(c) and (d), one of which is highlighted by an arrow. The γ' precipitates in the recrystallized region in Figures 7(c) and (d) are concentrated at the grain boundaries, and based on their size, shape, and distribution they cannot be identified with any of the γ' precipitate types present before forging.

For the highest strain region in sample D ($\varepsilon \approx 1.26$), a second large area EBSD map was captured, along with a corresponding FSE image to visualize γ' precipitates. This highlights that after compression the remaining large unrecrystallized grains contain predominately discontinuous γ' precipitates, indeed, in the IPF color-coded map shown in Figure 8, only one of the unrecrystallized grains contained octodendritic γ' precipitation.

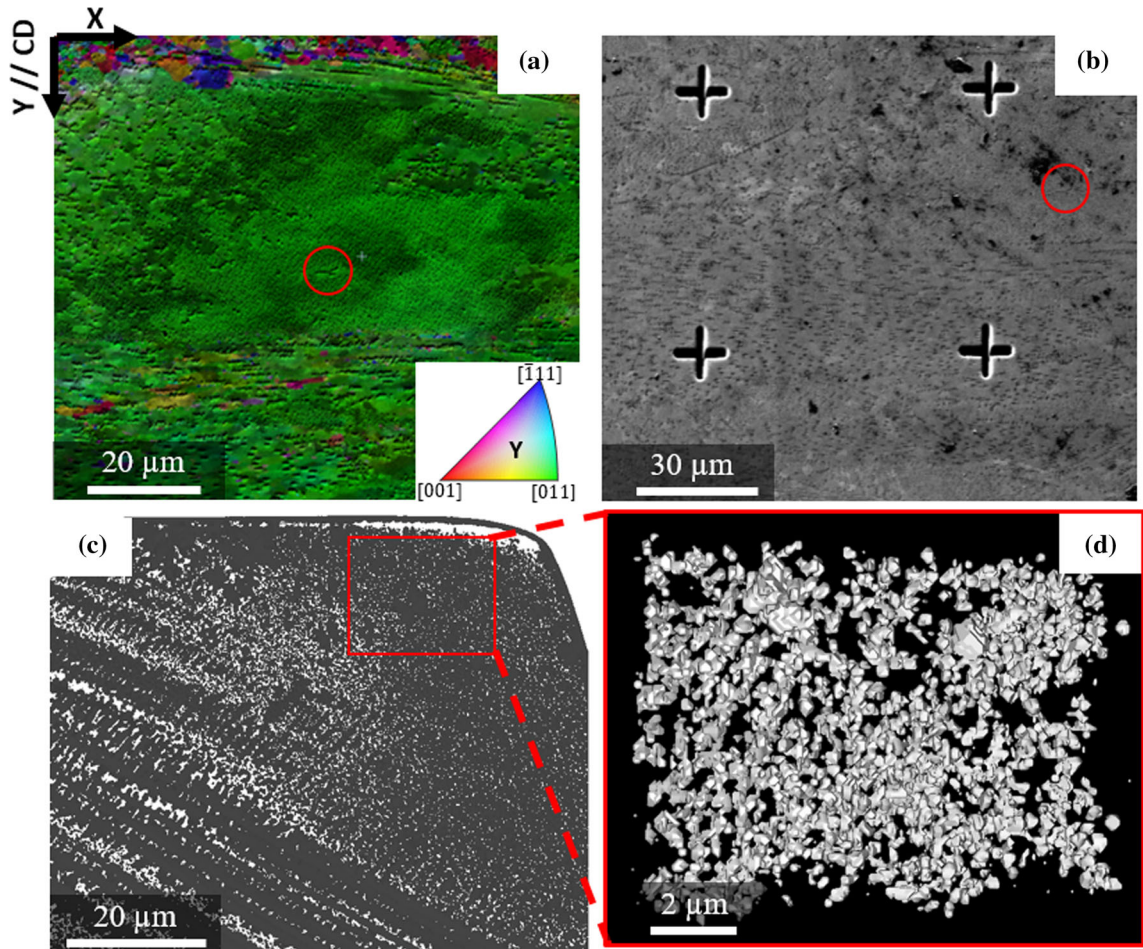


Fig. 9—A 3D view of dynamic γ' precipitation, obtained using FIB-SEM tomography. (a) BSE image of a region containing dynamically formed fine γ' precipitates with overlaid IPF map showing they are within a single grain, also containing octodendrites and discontinuous γ' precipitation, (b) SE image showing the markers used to delimit the region of interest, (c) 3D view of a segmented sub-volume, and (d) enlarged view of the dynamically formed γ' precipitates in (c). The red circles in (a) and (b) indicate a particular octodendritic γ' precipitate (Color figure online).

Additionally, a population of very fine and densely distributed spherical γ' precipitates can also be found in the remaining large unrecrystallized grains (arrowed on Figure 8(d)). The fine spherical γ' precipitates have only been observed after deformation, suggesting that they form during and after forging. FIB-SEM tomography was used to confirm that these dynamically formed γ' precipitates are indeed almost spherical in 3D, as can be seen in Figure 9.

IV. DISCUSSION

A. γ' Precipitation on Slow Cooling

Regarding intragranular γ' precipitation, two distinct categories of γ' precipitate have been identified following slow cooling, arising from (i) continuous and (ii) discontinuous precipitation. The continuous γ' precipitates adopt an octodendritic morphology, a shape which is known to be the result of precipitate coarsening.^[14,15] Initially, the γ' precipitates form with a spherical shape which minimizes their interfacial energy with the surrounding matrix. As they grow, strain energy builds up

due to the slight crystal lattice misfit between the γ and γ' phases, and the γ' precipitates develop a cuboidal morphology, with the cube edges along $\langle 100 \rangle$ directions, since these have the lowest elastic modulus. A detailed explanation for the splitting of cuboidal γ' precipitates was proposed by Cha *et al.*, based on a 2D phase field model of precipitate coarsening, which considered interfacial energy, strain energy, and solute gradients.^[24] This explanation is summarized as follows: The $\{100\}$ faces of cuboidal γ' precipitates become concave, as a result of faster growth along the $\langle 111 \rangle$ directions compared to the $\langle 100 \rangle$ directions, due to solute enrichment. The concave geometry leads to strain localization at the centers of the $\{100\}$ faces, and this drives dissolution of the γ' precipitates along the $\langle 100 \rangle$ directions, eventually splitting the cubes into octo-cubes. Coarsening continues at the outward facing corners of the octo-cubes, forming octodendrites, during which coherency between the γ' precipitate and matrix is lost, and the dendrite arms develop smoother interfaces with the matrix.^[15]

Morphologically, the discontinuous γ' precipitates present alternating branches of γ and γ' , and they

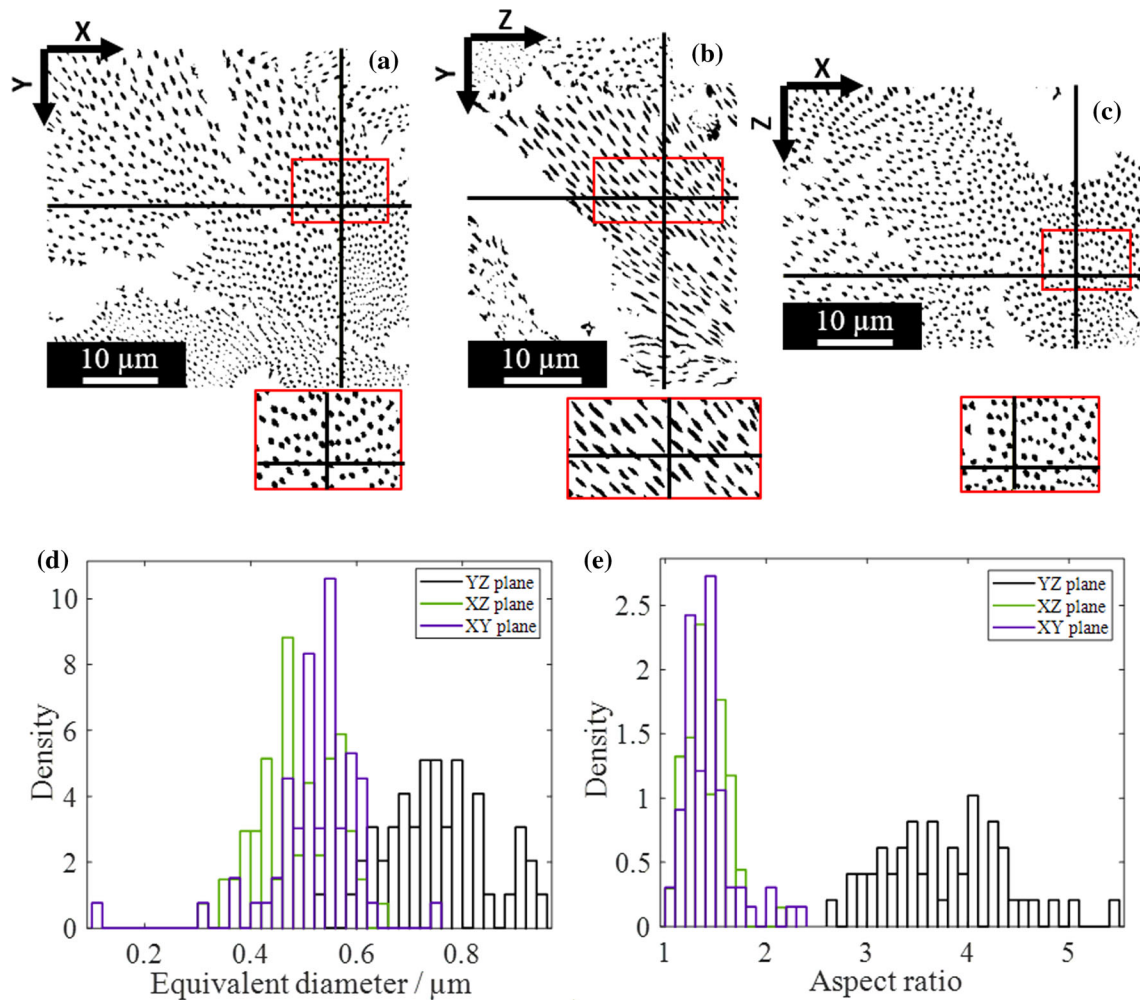


Fig. 10—The distribution of equivalent diameter and aspect ratio of the same γ' precipitates viewed from different planes. (a) to (c) A single point in a 3D dataset, indicated by the intersection of the black lines, viewed from XY, YZ, and XZ planes, respectively, (d) and (e) the size and aspect ratio distributions of ≈ 50 γ' precipitates, indicated in the red rectangles in (a) to (c) (Color figure online).

appear to form behind a moving grain boundary [e.g., Figure 3(b)]. Different formation mechanisms for discontinuous γ' precipitation have been proposed, but all have in common that they involve precipitation occurring at a grain boundary which acts as a reaction front and fast diffusion pathway.^[25,26] Mostly, these have precipitation occurring at moving grain boundaries, but the “pucker” mechanism suggested by Tu and Turnbull has precipitation inducing boundary motion.^[27]

In terms of their morphology, and forming behind a moving boundary, the discontinuous γ' precipitates are similar to the fan-type structures which have been reported to form in a number of Ni-based superalloys. An early example of the use of the term FTS was by Danflou *et al.* in 1996, where the growth kinetics of the fans was studied and used to confirm that they form discontinuously.^[28] A similar morphology had been identified by Henry *et al.* in 1993, though the term fan was not used to describe it.^[29] Subsequently, the name has been used in 1999 by Furrer *et al.*, who observed the formation of fan-type γ' precipitates during slow cooling of Udimet 720 (at a cooling rate of 0.12 °C/s).^[30] The

effect of cooling rate on fan the size and spacing of fan-type γ' precipitates has been investigated by Mitchell *et al.*^[10] and Hu *et al.*,^[13] with both finding that slower cooling rates lead to larger FTS, with larger spacing between the fans, *i.e.*, between the branches of γ' .

Most recently, Atrazhev *et al.* have given a detailed model for the formation of fan-type γ' precipitates, and shown that grain boundary mobility is the key factor favoring their formation.^[16] When grain boundary mobility is high, the formation of FTS behind moving boundaries is favored. When it is lower, grain boundary γ' precipitates form and cause grain boundary serrations to develop. As a consequence, slow cooling rates in the vicinity of the solvus temperature favor the formation of FTS.

Thermodynamically, the grain boundary motion which is accompanied by discontinuous and fan-type γ' precipitation can be driven by the free energy change of decomposition of the supersaturated γ matrix ahead of the advancing boundary.^[16,31] This driving force is relevant in the present case, where there is little driving force from capillarity [*i.e.*, due to the coarse-grained

starting microstructure, shown in Figure 2(a)], and little driving force from stored strain energy [shown in Figure 2(d)].

Although an example of a FTS is highlighted in Figure 5(c), the majority of the discontinuous γ' precipitation observed in this study [and in Figure 5(c)] was not considered to be FTS. While similar in terms of forming discontinuously behind a moving boundary and presenting alternating branches of γ and γ' , it is different in that the majority of the γ' precipitation here does not appear to originate from a single grain boundary precipitate. Additionally, it was not found behind curved grain boundaries, but can be found behind very flat boundary sections [see Figure 3(b)].

As shown in Figure 5, this discontinuous γ' precipitation can exhibit different shapes in 2D sections, depending on how it intersects the section under investigation (*i.e.*, the plane of view). This can interfere with the measurements of γ' precipitate size and shape, as highlighted in Figure 10. This figure uses a 3D sub-volume from the area shown in Figure 5. A particular point in this sub-volume (indicated by the intersection of the black lines) is viewed from three perpendicular planes. The size and aspect ratio of approximately 50 γ' precipitates surrounding this point (highlighted by the red rectangles) were measured. While these were quite similar in the XY and XZ plane, with equivalent circle diameters $\approx 0.49 \mu\text{m}$ and aspect ratios ≈ 1.42 , the equivalent diameter shown in the YZ plane is 50 pct higher at $0.75 \mu\text{m}$, and the aspect ratio more than twice as much at 3.76. From this analysis it is clear, and one should keep in mind, that the analysis of γ' precipitate size and shape must be done with great care in the case of such anisotropic systems. Observations made in 2D sections can indeed be very misleading when dealing with such very elongated γ' precipitate shapes.

Additionally, it was noted in Figure 3 that grain boundary γ' precipitates are found. When these coincided with the discontinuous precipitation reaction front some very flat grain boundary sections were found [*i.e.*, Figure 3(b)]. Some very striking straight lines of intragranular γ' precipitation were also found [*i.e.*, the red circled area in Figure 3(b)], and these are likely to be a consequence of the “stop and go” movement of the discontinuous precipitation reaction front, indicating where a migrating boundary has previously stopped^[32]. Figure 3(b) appears to show that the boundary can begin moving again while leaving behind the discontinuous reaction front.

B. Interaction Between γ' Precipitates and Recrystallization During Forging

As discussed earlier, at the start of forging, the microstructure comprises a mixture of octodendrites and discontinuous γ' precipitates along with grain boundary precipitates. Figure 7 shows that the recrystallized grains which form have γ' precipitates concentrated at their boundaries. These γ' precipitates cannot be identified with either the octodendritic or the discontinuous γ' precipitation. This implies two possibilities; firstly, these γ' precipitates may be remaining fragments

of the initial γ' precipitation, or the recrystallized grains may have (partially) dissolved the initial γ' precipitation, and reprecipitation has occurred at their boundaries, which had become rich in the γ' forming elements. There being no fragments of initial γ' precipitation in the recrystallized grains implies that during recrystallization the recrystallized grains at least partially dissolve the γ' precipitates which they encounter, whether they be octodendritic or discontinuous.

As shown in Figures 8 and 9, a third population of intragranular γ' precipitate was identified in the unre-crystallized grains after forging, suggesting their dynamic formation during forging. These dynamically forming γ' precipitates appear to be small, densely distributed, and spherical. Recrystallization must overcome all three types of intragranular γ' precipitation if it is to progress.

Figure 11 shows the progression of recrystallization in a region with octodendritic γ' precipitation. A segmented version of the BSE image in Figure 11(a) is shown in (c), where the γ' precipitates appear as black pixels, and the matrix as white. The distance transform was applied to Figure 11(c) to produce Figure 11(d). This transform colorizes each pixel according to the distance from that pixel to the nearest black pixel (*i.e.*, the nearest γ' precipitate). Figure 11(c) shows that the regions enclosed by the red and black boxes in (b) both contain similar octodendritic γ' precipitation. Despite this similarity, recrystallization is more advanced in the region enclosed by the black box, likely due to there being more dislocation activity in this region. This can be explained by the different textures of the grains in the two regions, and different plastic incompatibilities with their neighboring grains.

Inspecting Figures 11(e) and (f) allows the progression of recrystallization in regions with octodendritic γ' precipitates to be inspected. In the early stages of recrystallization, dislocations pile up at the γ/γ' interfaces. This is evidenced by the medium angle grain boundaries (MAGBs) being concentrated at these interfaces in Figure 11(e). MAGBs are here defined as boundaries with misorientation angles between 5° and 10° ; they correspond to dislocation arrays and are plotted blue. Towards the top left of Figure 11(f) sub-grains (enclosed by MAGBs) have formed; these have no internal γ' precipitates, and their boundaries are decorated by γ' precipitates. The blue arrows indicate two such sub-grains. Towards the bottom right of Figure 11(f) two fully formed recrystallized grains (enclosed by HAGBs) are indicated by the black arrows. From Figures 11(e) and (f) the stages of recrystallization in regions with octodendritic γ' precipitation can be suggested as follows:

Initially, dislocations pile up at the γ/γ' interfaces, indicated by the MAGBs in Figure 11(e). With further deformation, dislocation walls branch out from the γ/γ' interfaces and form enclosed sub-grains (enclosed by MAGBs) between the precipitates and may partially dissolve the γ' precipitates they encounter [Figure 11(f), blue arrows]. As more dislocations are accumulated into these sub-boundaries they increase their misorientation angle and develop into high-angle boundaries, enclosing

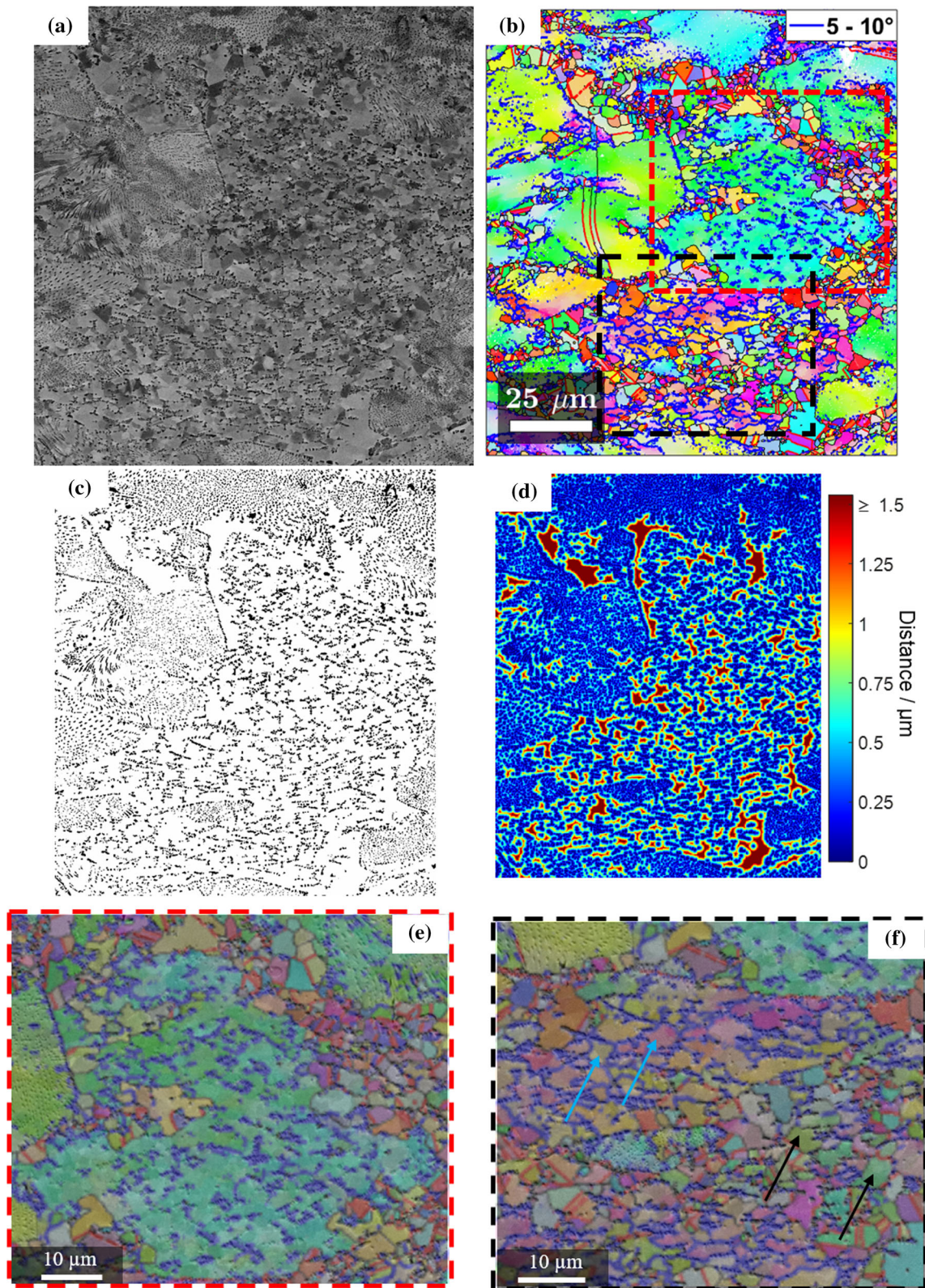


Fig. 11—Recrystallization around octodendritic γ' precipitates in sample D, under a local strain of $\epsilon \approx 0.95$. (a), (b) A BSE image and its corresponding IPF Y map with overlaid medium angle grain boundaries (5 to 10 deg misorientation angles, plotted blue), respectively, (c) segmented version of (a) with γ' precipitates plotted black and (d) the distance transform applied to (c). (e) and (f) higher magnification FSE images of the areas outlined in red and black, respectively, in (b), containing octodendrites and showing different stages of recrystallization (Color figure online).

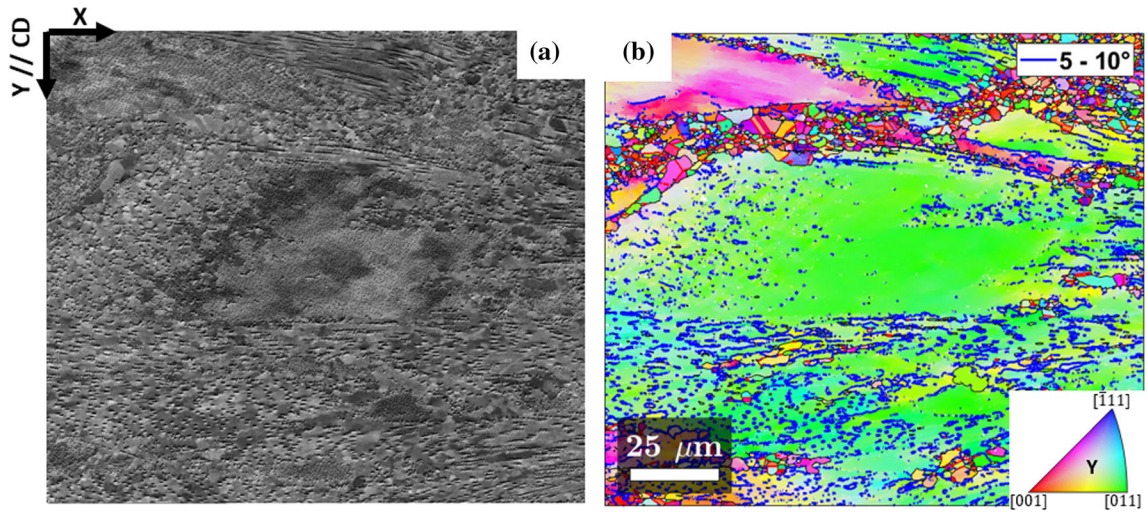


Fig. 12—(a) An FSE image and (b) its corresponding IPF Y map with overlaid MAGBs of a region containing dynamic γ' precipitation where the local strain was $\varepsilon \approx 1.15$.

recrystallized grains with no internal γ' precipitation [Figure 11(f), black arrows].

As highlighted in Figure 8, recrystallization is more advanced in regions with octodendritic precipitates than those with discontinuous γ' precipitates. The observed difference in recrystallization behavior can be explained using a model proposed by Humpherys.^[33] In this model, sub-grains are considered to form in a region with an orientation gradient Ω deg/ μm . If this region contains precipitates (as in the present case), the size of the sub-grains which form is limited to approximately the spacing between the precipitates (D). When the sub-grains are limited to a diameter D , they can form a boundary with a misorientation angle of approximately $\theta = \Omega * D$ to their surrounding grain. If this is above the threshold for a (high mobility) HAGB, a recrystallized grain can form. Thus, in this model, recrystallization is favored in regions with high misorientation gradients (*i.e.*, high applied strain) and regions where large sub-grains can form (*i.e.*, regions where γ' precipitates are spaced far apart).

The key influence of precipitation on recrystallization, based on these considerations, is that they limit sub-grain size to approximately the inter-particle spacing. The precipitate limited sub-grain size can be *estimated* analytically, as a function of the precipitate volume fraction, their size, and a geometric factor. For example, for a cubic arrangement of spherical precipitates, the particle spacing is given by

$$D = \left(\frac{4\pi}{3}\right)^{\frac{1}{3}} * \left(\frac{r^3}{f}\right)^{\frac{1}{3}}. \quad [1]$$

Here, the first term is the geometrical factor and evaluates to 1.61, and the second is related to the precipitates' size and volume fraction. Experimental measurements of particle limited grain size can be fit to Eq. [1], with estimates for the geometric factor ranging from 2.7 to 3.6.^[33]

In the present case, appropriate values of both the geometric factor and of precipitate size cannot be easily estimated, given the irregular precipitate shapes.

However, using segmented images, a proxy measure for the precipitate limited sub-grain size can be calculated directly from the images, and used to compare the relative ease of sub-grain formation in different regions. This proxy measure is based on applying the distance transform to segmented images of the γ' precipitation, and is shown in Figure 11(d). The segmentation is not perfect; some very dark γ grains are labeled as precipitates, and *vice versa* some very faint γ' precipitates are labeled as matrix. Overall, the segmentation is still reasonably good. The color scale in Figure 11(d) has been limited to 1.5 μm , to maximize the contrast between regions with octodendritic and discontinuous γ' precipitation.

The central region of the micrograph presented in Figure 11, which contains the octodendrites, shows higher values of inter-precipitate spacing than the surrounding grains containing discontinuous γ' precipitates. According to the model described above, these higher values should favor the formation of recrystallized grains in regions with octodendritic γ' precipitation compared to regions with discontinuous γ' precipitation.

C. Dynamic Precipitation

On the basis of the above discussion, the dynamically forming γ' precipitates can be expected to pose a significant barrier to recrystallization, due to the very small inter-precipitate spacing, preventing the formation of intragranular MAGBs which may act as recrystallization nuclei. This effect is shown in Figure 12 where it can be seen that in the region of the grain containing dynamic γ' precipitation, no MAGBs have formed, whereas in other parts of the grain, MAGBs have formed at the γ/γ' interfaces.

The phenomena of dynamic precipitation have been observed previously in different alloy systems, including MnS precipitates in steels^[34] and Nb(C,N) in steels.^[35] In DSC experiments, deformation at 800 °C was shown to lower the temperature of the exothermic peak associated with precipitation of γ'' in IN718 from 804 °C to 742 °C.^[36] It is worth noting that in these cases, dynamic precipitation seems to have occurred uniformly throughout the microstructure, whereas here these γ' precipitates were only found in certain regions of some unrecrystallized grains.

This phenomenon is explained as follows. During deformation, dislocation density increases, and the dislocations become entangled with one another. Precipitation along the dislocation line is energetically favorable, due to the interaction between the strain field of the dislocation and that of the precipitate. Such interactions are complex, and for the purposes of modeling dynamic precipitation they can be simplified to the assumption that precipitation along the dislocation releases the dislocation core energy over the precipitate radius, as done by Dutta *et al.*^[35,37]

Due to recrystallization, and dislocation trapping by precipitates, sample D in this study is not expected to have a uniform distribution of dislocations, and certain high dislocation density regions with a higher density of dislocation nodes are the favored sites for dynamic γ' precipitation. Dutta *et al.* have shown that a non-uniform distribution of dislocations in the matrix of metal-matrix composites leads to different precipitation kinetics than in the pure matrix material.^[38] In the present case, higher dislocation densities in the unrecrystallized grains favor dynamic precipitation there, rather than in the recrystallized grains.

V. CONCLUSIONS

In this work, the γ' precipitate state that develops during *slow* cooling of a γ - γ' nickel-based superalloy from supersolvus temperatures and its interaction with recrystallization were described. The main conclusions are as follows:

- When cooling through the solvus temperature, at cooling rates representative of industrial billet conversion process, a mixture of continuous and discontinuous precipitates forms. The continuous γ' precipitation coarsens to form octodendrites, and the discontinuous γ' precipitates form behind moving grain boundaries with a very elongated (called here “spaghetti”) morphology.
- 3D FIB-tomography shows that such discontinuous elongated γ' precipitates present significantly different shapes and sizes depending on the plane from which they are viewed, potentially leading to unreliable measures of precipitate size and shape based solely on 2D micrographs.
- Regions with continuous γ' precipitation present less of a barrier to recrystallization than regions with discontinuous γ' precipitation, and this difference can be rationalized based on the inter-precipitate

spacing. Neither type of γ' precipitate was found in dynamically recrystallized areas after subsolvus compression, implying that both were dissolved by the recrystallization front.

- Dynamic γ' precipitates were found to form during subsolvus forging, and these strongly inhibit recrystallization, by limiting sub-grain size and sub-boundary misorientation and thus hindering the formation of recrystallization nuclei.

ACKNOWLEDGEMENTS

The authors would like to acknowledge the support provided by Aubert & Duval, and by the Advanced Forming Research Centre (AFRC), University of Strathclyde, which receives partial funding from the UK’s High Value Manufacturing CATAPULT.

CONFLICT OF INTEREST

On behalf of all authors, the corresponding author states that there is no conflict of interest.

OPEN ACCESS

This article is licensed under a Creative Commons Attribution 4.0 International License, which permits use, sharing, adaptation, distribution and reproduction in any medium or format, as long as you give appropriate credit to the original author(s) and the source, provide a link to the Creative Commons licence, and indicate if changes were made. The images or other third party material in this article are included in the article’s Creative Commons licence, unless indicated otherwise in a credit line to the material. If material is not included in the article’s Creative Commons licence and your intended use is not permitted by statutory regulation or exceeds the permitted use, you will need to obtain permission directly from the copyright holder. To view a copy of this licence, visit <http://creativecommons.org/licenses/by/4.0/>.

SUPPLEMENTARY INFORMATION

The online version contains supplementary material available at <https://doi.org/10.1007/s11661-022-06878-w>.

REFERENCES

1. R.C. Reed: *The Superalloys: Fundamentals and Applications*, Cambridge University Press, Cambridge, 2006.

2. R.R. Unocic, G.B. Viswanathan, P.M. Sarosi, S. Karthikeyan, J. Li, and M.J. Mills: *Mater. Sci. Eng. A*, 2008, vol. 483–84, pp. 25–32.
3. D.M. Collins and H.J. Stone: *Int. J. Plast.*, 2014, vol. 54, pp. 96–112.
4. M.P. Jackson and R.C. Reed: *Mater. Sci. Eng. A*, 1999, vol. 259, pp. 85–97.
5. R.W. Kozar, A. Suzuki, W.W. Milligan, J.J. Schirra, M.F. Savage, and T.M. Pollock: *Metall. Mater. Trans. A*, 2009, vol. 40A, pp. 1588–603.
6. F. Masoumi, M. Jahazi, D. Shahriari, and J. Cormier: *J. Alloy. Compd.*, 2016, vol. 658, pp. 981–95.
7. F. Masoumi, D. Shahriari, M. Jahazi, J. Cormier, and A. Devaux: *Sci. Rep.*, 2016, vol. 6, p. 16.
8. F. Masoumi, M. Jahazi, J. Cormier, and D. Shahriari, in *2nd European Symposium on Superalloys and their Applications*, E D P Sciences, Giens, France, 2014.
9. A.J. Ardell: *Acta Metall.*, 1968, vol. 16, pp. 511–16.
10. R.J. Mitchell, H.Y. Li, and Z.W. Huang: *J. Mater. Process. Technol.*, 2009, vol. 209, pp. 1011–17.
11. A. Coyne-Grell, J. Blaizot, S. Rahimi, I. Violatos, S. Nouveau, C. Dumont, A. Nicolaş, and N. Bozzolo: *J. Alloy. Compd.*, 2022, vol. 916, 165465.
12. M. Pérez, C. Dumont, and S. Nouveau, in *The 14th International Symposium on Superalloys (Superalloys 2021)* eds. S. Tin, M. Hardy, J. Clews, J. Cormier, Q. Feng, J. Marcin, C. O'Brien and A. Suzuki, 2020, pp. 441–49.
13. B.F. Hu, G.Q. Liu, K. Wu, and P.H. Hu: *Acta Metall. Sin.*, 2012, vol. 48, pp. 830–36.
14. R.A. Ricks, A.J. Porter, and R.C. Ecob: *Acta Metall.*, 1983, vol. 31, pp. 43–53.
15. T. Grosdidier, A. Hazotte, and A. Simon: *Mater. Sci. Eng. A*, 1998, vol. 256, pp. 183–96.
16. V.V. Atrazhev, S.F. Burlatsky, D.V. Dmitriev, D. Furrer, N.Y. Kuzminyh, I.L. Lomaev, D.L. Novikov, S. Stolz, and P. Reynolds: *Metall. Mater. Trans. A.*, 2020, vol. 51A, pp. 3648–57.
17. A. Devaux, B. Picque, M.F. Gervais, E. Georges, T. Poulain, and P. Heritier: *Superalloys*, 2012, vol. 2012, pp. 911–19.
18. M. Kulakov, S. Rahimi, and S.L. Semiatin: *Metall. Mater. Trans. A.*, 2022, vol. 53A, pp. 407–19.
19. S. Berg, D. Kutra, T. Kroeger, C.N. Straehle, B.X. Kausler, C. Haubold, M. Schiegg, J. Ales, T. Beier, M. Rudy, K. Eren, J.I. Cervantes, B.T. Xu, F. Beuttenmueller, A. Wolny, C. Zhang, U. Koethe, F.A. Hamprecht, and A. Kreshuk: *Nat. Methods*, 2019, vol. 16, pp. 1226–32.
20. J. Schindelin, I. Arganda-Carreras, E. Frise, V. Kaynig, M. Longair, T. Pietzsch, S. Preibisch, C. Rueden, S. Saalfeld, B. Schmid, J.Y. Tinevez, D.J. White, V. Hartenstein, K. Eliceiri, P. Tomancak, and A. Cardona: *Nat. Methods*, 2012, vol. 9, pp. 676–82.
21. A.J. Wilkinson and P.B. Hirsch: *Micron*, 1997, vol. 28, pp. 279–308.
22. A. Nicolay, J.M. Franchet, J. Cormier, H. Mansour, M. De Graef, A. Seret, and N. Bozzolo: *J. Microsc.*, 2019, vol. 273, pp. 135–47.
23. F. Kocks, C. Tomè, and H. R. Wenk, *Texture and Anisotropy. Preferred Orientations in Polycrystals and Their Effect on Material Properties*, 2000.
24. P.R. Cha, D.H. Yeon, and S.H. Chung: *Scripta Mater.*, 2005, vol. 52, pp. 1241–45.
25. F. Findik: *J. Mater. Sci. Lett.*, 1998, vol. 17, pp. 79–83.
26. P. Zieba: *Arch. Metall. Mater.*, 2017, vol. 62, pp. 955–68.
27. K.N. Tu and D. Turnbull: *Acta Metall.*, 1967, vol. 15, pp. 1317–23.
28. H. Danflou, M. Macia, T. Sanders and T. Khan, 1996.
29. M.F. Henry, Y.S. Yoo, D.Y. Yoon, and J. Choi: *Metall. Trans. A*, 1993, vol. 24, pp. 1733–43.
30. D.U. Furrer and H.J. Fecht: *Scripta Mater.*, 1999, vol. 40, pp. 1215–20.
31. J.W. Cahn: *Acta Metall.*, 1959, vol. 7, pp. 18–28.
32. M. Chronowski and P. Zięba: *Arch. Civ. Mech. Eng.*, 2020, vol. 20, p. 35.
33. J. Humphreys, G.S. Rohrer, and A. Rollett: *Recrystallization and Related Annealing Phenomena*, 3rd ed. Elsevier Science Bv, Amsterdam, 2017, pp. 1–704.
34. F. H. An, D. Q. Zhang, and P. T. Feng, *Steel Research International*, 2021, **92**.
35. B. Dutta, E. Valdes, and C.M. Sellars: *Acta Metall. Mater.*, 1992, vol. 40, pp. 653–62.
36. H.J. Zhang, C. Li, Y.C. Liu, Q.Y. Guo, Y. Huang, H.J. Li, and J.X. Yu: *J. Alloy. Compd.*, 2017, vol. 716, pp. 65–72.
37. B. Dutta, E. Palmiere, and C.M. Sellars: *Acta Mater.*, 2006, vol. 49, pp. 785–94.
38. I. Dutta and D.L. Bourell: *Acta Metall. Mater.*, 1990, vol. 38, pp. 2041–49.

Publisher's Note Springer Nature remains neutral with regard to jurisdictional claims in published maps and institutional affiliations.